Advances in Water Resources 180 (2023) 104522

Contents lists available at ScienceDirect

Advances in Water Resources

journal homepage: www.elsevier.com/locate/advwatres

Solute transport in highly heterogeneous media: The asymptotic signature of connectivity

Anthony Beaudoin [a], Iván Colecchio [b,c], Alejandro Boschan [b,c,*]

[a] Institute of Pprime, SP2MI - Téléport 2, Boulevard Marie et Pierre Curie, BP 30179, 86962 Futuroscope Chasseneuil Cedex, France
[b] Grupo de Medios Porosos, Facultad de Ingeniería, Universidad de Buenos Aires, Paseo Colón 850, Buenos Aires, Argentina
[c] CONICET, Buenos Aires, Argentina

ARTICLE INFO

Keywords:
Percolation
Dispersivity
Binary media
Stochastic

ABSTRACT

The connectivity of the more conductive hydrofacies strongly determines flow and transport in heterogeneous media. Here we study solute transport in 3D binary isotropic samples with a proportion p of a high hydraulic conductivity facies (k^+), and $(1-p)$ of a low (k^-) one. The k^+ facies is characterized by two connectivity parameters: a connectivity structure type (no, low, intermediate and high), that controls how well the k^+ facies is connected, and an integral scale I_b, that controls the heterogeneity characteristic lengthscale. Under ergodic conditions, and in the asymptotic Fickian regime that arises only very far from the injection plane, we analyze two transport quantities: the normalized mean solute arrival time $\langle t_a^* \rangle$, and the longitudinal dispersivity α_L. As p reaches the percolation threshold p_c (p_c depends on the connectivity parameters), k^+ channels spanning the sample along the mean flow direction appear, giving rise to fast flow pathways . A sharp decrease of $\langle t_a^* \rangle$, and a sharp increase of α_L, occur when $p \to p_c$. As p exceeds p_c, a subsequent minimum of $\langle t_a^* \rangle$ and a maximum of α_L are observed. This result is in contrast with previous ones by other authors that found a maximum of α_L at $p = p_c$. On the other hand, p kept fixed, α_L decreases as the connectivity of the k^+ facies increases. We conclude that the connectivity features sampled by the solute particles during their trajectories are retained in the transport quantities even after the asymptotic regime is attained. Also, that connectivity mainly affects α_L through a shift or displacement of p_c. Finally, the existence of a spatial connectivity structure may imply early, but also late, arrival times, compared with the absence of structure.

1. Introduction

The study of the mechanisms involved in the transport of solutes in heterogeneous porous media is central in a variety of scientific and technological applications such as the groundwater and soil remediation, underground hydrogen storage, geological radioactive waste storage, geothermal energy production, mining and oil and gas recovery (Bradley et al., 2023; Dentz et al., 2023; Lester et al., 2023; Kong et al., 2023).

Our knowledge of the subsurface is intrinsically incomplete due to the scarcity of field measurements. The related uncertainty is frequently mitigated by the use of stochastic approaches, in which random space functions (RSF) are constructed to describe the heterogeneity of a medium, not as a single deterministic image, but as an ensamble of images (Dagan, 1989). Among the RSF, Multi-Gaussian fields (Freeze, 1975; Gelhar, 1986; de Dreuzy et al., 2007) are the most widely studied. In these, the point values of hydraulic conductivity $k(\bar{r})$ are the result of a random process with a unimodal Gaussian probability density function $P(\ln(k(\bar{r})))$, with mean $\langle \ln(k(\bar{r})) \rangle$, and variance $\sigma^2_{\ln(k(\bar{r}))}$, while the spatial correlation of $k(\bar{r})$ is defined by a covariance function $\rho(k(\bar{r}))$ with a certain integral length scale I. Typically, $0 < \sigma^2_{\ln(k(\bar{r}))} < 0.5$ represents a mild degree of heterogeneity, while $2 < \sigma^2_{\ln(k(\bar{r}))} < 9$ a high one. However, for media composed of regions or domains with components of highly differing flow properties, the Multi-Gaussian representation might be inaccurate (Rubin, 1995; Huang and Dai, 2008). For example, alluvial fan systems (Fleckenstein and Fogg, 2008), or fluvio-glacial deposits (De Caro et al., 2020) may present a structure of interconnected geobodies (e.g. sandy/gravel lenses with a clay/sandstone matrix) (Fogg, 1986; Journel and Alabert, 1989; Guin and Ritzi, 2008), that are far from unimodal, and require a more realistic representation in terms of multiple hydrofacies. In all cases, the connectivity of the more conductive components strongly impacts flow and transport in a way that is not always captured by $P(k(\bar{r}))$ and $\rho(k(\bar{r}))$ (Poeter and Townsend, 1994; Zappa et al., 2006). The spatial variability of the flow velocity fields over scales from the pore scale

* Corresponding author at: Grupo de Medios Porosos, Facultad de Ingeniería, Universidad de Buenos Aires, Paseo Colón 850, Buenos Aires, Argentina.
E-mail address: abosch@fi.uba.ar (A. Boschan).

https://doi.org/10.1016/j.advwatres.2023.104522
Received 6 May 2023; Received in revised form 11 August 2023; Accepted 18 August 2023
Available online 22 August 2023

Nomenclature

List of acronyms

HCS	High connectivity structure
LCS	Low connectivity structure
NS	No structure
NST	Normal score transform
BTC	Breakthrough curve
RSF	Random space function

List of symbols

Δ	Grid cell linear size
$k(\bar{r})$	Point values of hydraulic conductivity
$k_i(\bar{r})$	Intermediate indicator
k^+, k^-	Characteristic conductivity of the facies
K_{eq}	Equivalent hydraulic conductivity
$\rho(\bar{r})$	Covariance function
L_x, L_y, L_z	Sample linear size
I	Underlying integral scale (multigausssian samples)
I_b	Binary media integral scale
$\langle \ln(k(\bar{r}))\rangle$	Mean of the hydraulic conductivity distribution
p	Proportion of a high conductivity facies
p_c	Percolation threshold of the high conductivity facies
$\Delta h/L_x$	Hydraulic head gradient
U_x	Mean flow velocity
u_x, u_y, u_z	Components of the flow velocity field
D_m	Solute molecular diffusion coefficient
t_a	Arrival time of the solute particles
t_a^*	Dimensionless arrival time
α_L	Longitudinal solute dispersivity
$P(k(\bar{r}))$	Hydraulic conductivity probability density function
$\sigma_{\ln k(\bar{r})}$	Variance of the natural logarithm of the hydraulic conductivity distribution
Δx^2	Second moment of the solute particle spatial distribution
t	Time
τ_D	Characteristic diffusion time
τ_A	Characteristic advection time

to the aquifer scale gives rise to several mechanisms of dispersion of a solute. Moreover, tortuous fast flow pathways (channeling) can lead to significant variations of first arrival times and spreading of a contaminant (Western et al., 2001; Knudby et al., 2006; Bianchi and Zheng, 2016; Molinari et al., 2019). In this regard, a binary representation, obtained through the regrouping of multiple hydrofacies into two main ones, is an appropriate frameset to study the behavior of flow and transport at the onset of channeling: it makes it possible to retain the geometrical complexity of the fast flow pathways, and to use the point of view of percolation theory to analyze them, while it maintains the parameter space tractable.

1.1. Connectivity and flow

Mean flow parameters, such as the equivalent conductivity K_{eq}, are highly dependent on the connectivity of the high $k(\bar{r})$ classes, facies or components. In the following, we use the term " classes" for continuous $k(\bar{r})$ distributions (e.g. Multigaussian), "facies" for discrete ones (e.g. binary), and "components" in general. Several works revised connectivity metrics and their use to predict these parameters (Knudby et al., 2006; Renard and Allard, 2013), finding strong correlations between some of these metrics and K_{eq}. For multigaussian media, the intermediate $k(\bar{r})$ classes form a connected network, while the high and low $k(\bar{r})$ classes form isolated blobs. In order to take into account a wider range of connectivity scenarios, (Zinn and Harvey, 2003) applied a normal score transform (NST) to multigaussian media, performing this way a spatial swap, after which it is the high $k(\bar{r})$ classes that form a connected network (or isolated blobs). Otherwise said, after the NST, high $k(\bar{r})$ classes will have an increased or reduced connectivity (here called high or low connectivity structure), thus representing extreme cases of connectivity for an isotropic $k(\bar{r})$ field, $P(\ln(k(\bar{r})))$, $\langle\ln(k(\bar{r}))\rangle$, $\sigma^2_{\ln(k(\bar{r}))}$ and $\rho(k(\bar{r}))$ kept fixed. The NST is a simple transformation that maintains the gaussianity of $P(k(\bar{r}))$ and the shape of $\rho(k(\bar{r}))$ (while I changes). Zinn and Harvey used these media to study K_{eq} in 2D, finding, for the high and the low connectivity structures respectively, greater and smaller K_{eq} than for the original multigaussian media. Later, Jankovic et al. (2016), analyzed the K_{eq} of such structures in 3D, finding a much smaller contrast of K_{eq}, between the high and low connectivity structures, than in 2D.

Colecchio et al. (2021) followed a similar approach on binary media with a k^+ and a k^- facies, using 2D and 3D samples for which the k^+ facies could have no, low, intermediate or high connectivity structure. The authors found that any influence of connectivity on K_{eq} could be well accounted for simply by a shift in the percolation threshold p_c of the k^+ facies. Previously, the connectivity of 2D binary media made of inclusions was studied by Knudby et al. (2006) by using an empirical formula to estimate K_{eq}, while McKenna et al. (2011) analyzed K_{eq} for 2D truncated multigaussian fields with a distance-based upscaling procedure, finding a strong dependence of K_{eq} on the percolation threshold p_c if the k^+/k^- contrast is high. So did (Boschan and Noetinger, 2012) in 3D. Oriani and Renard (2014) used image analysis over binary samples to evaluate a new connectivity metric, the solidity indicator, that was found to be very well correlated to K_{eq} in 2D.

1.2. Connectivity and transport

Connectivity also controls the parameters and regimes of the transport of a passive solute, as high $k(\bar{r})$ channels or low $k(\bar{r})$ barriers make for the interplay between fast flow pathways and slow retention zones, that drive the arrival times and spreading of the solute (Edery et al., 2014). This is why identifying the relationship among connectivity and transport quantities such as mean arrival times and dispersivity is crucial for uncertainty management and risk assessment (Tyukhova et al., 2015; Rizzo and de Barros, 2017, 2019). However, deriving these quantities directly from properties of heterogeneous media still remains a major challenge (Bradley et al., 2023; Cirpka et al., 2022; Dentz et al., 2023; Talon et al., 2023). For weakly heterogeneous media, a First Order Approximation predicts that longitudinal dispersivity α_L attains an asymptotic value given by $\alpha_L = I\sigma^2_{\ln(k(\bar{r}))}$ (Fiori et al., 2017).

Here $\alpha_L = D_L/U_x$, where D_L is the longitudinal dispersion coefficient and U_x the mean flow velocity. As heterogeneity increases, the asymptotic regime is more rarely attained, and anomalous (Non-Fickian) transport starts to prevail. Indeed, this kind of behavior was reported to occur in very simple types of media, such as layered ones (Matheron and De Marsily, 1980) (for parallel flow). Anomalous transport has been extensively described from the theoretical and numerical point of view, (Berkowitz and Scher, 1995, 1997), for field data (Sidle et al., 1998; Gouze et al., 2008; Ben-Noah et al., 2023; Bianchi et al., 2023) and laboratory experiments (Moroni et al., 2007; Tyukhova and Willmann, 2016). For media with large variances, strong tailing, driven by advection through low conductivity regions, was observed (as later Willmann et al. (2008) and Srzic et al. (2013) did). Moreover, anomalous transport in highly heterogeneous media is frequently explained by incomplete mixing (Le Borgne et al., 2011). However, for very far monitoring distances, when the solute particles have sampled thoroughly the heterogeneity characteristic features (Zarlenga and Fiori, 2015), transport evolves slowly from anomalous to normal, the asymptotic Fickian regime is achieved (Jankovic et al., 2006; Fiori et al., 2017), and dispersivity parameters can be well-characterized (de Dreuzy et al., 2007; Beaudoin and de Dreuzy, 2013).

Zinn and Harvey (2003) also analyzed the behavior of D_L in their work, finding that it was respectively greater and smaller for the high and low connectivity structures than for multigaussian media. Indeed, they evaluated that, in their "connected" media, D_L behaved as in the layered media of Matheron and De Marsily (1980), for parallel flow, despite the fact that the two types of media are topologically very different. In contrast with their 2D results, the 3D simulations performed by Jankovic et al. (2016) yielded breakthrough curves (BTC) that were "practically independent" of the (connectivity) structure, which is a remarkable result, in the light of other studies that showed that the fastest pathways, i.e the "least resistance path" (Tyukhova et al., 2015; Rizzo and de Barros, 2017, 2019), are strongly correlated to the first arrival time of the solute.

A considerable branch of studies on transport have been carried out in the framework of percolation theory, which provides quantitative measures of connectivity (Renard and Allard, 2013). Dispersion D_L follows a percolation power law scaling (Sahimi, 1987; Koplik et al., 1988), that depends on whether the "dead ends" of the flow backbone significantly contribute to dispersion or not. Later, it was shown that these scaling laws are appropriate for anomalous transport (Sahimi, 2012). Finally, Rivard and Delay (2004) studied the behavior of the longitudinal dispersion coefficient D_L, in 2D percolative networks with a proportion p of conductive bonds. They observed that D_L increased sharply with the proportion p, and then decreased, with a maximum at $p \approx p_c$.

1.3. Objectives

The present article conveys some of the issues addressed in a previous article (Colecchio et al., 2021), that studied the influence of connectivity and percolation on flow parameters, to the more complex domain of solute transport. Considering highly heterogeneous 3D media: is there any remaining influence of the connectivity features sampled by the solute particles during their trajectories on the transport quantities once the asymptotic regime is attained ? How does the onset and completion of percolation affect mean arrival times and dispersivity in this situation? In that regard, by following a stochastic approach, we have performed simulations of advective–diffusive transport on very long and heterogeneous random binary samples, analyzing, under ergodic conditions, the spatial statistics of the solute particle cloud in the asymptotic regime that arises only very far from the injection plane. Connectivity was modified explicitly by varying the connectivity structure type and the integral scale I_b (these are the connectivity parameters that control the spatial organization of the k^+ component or facies), but also varies implicitly with its proportion p. Spatially uncorrelated media samples were used as a reference of the absence of connectivity structure. Due to the non-trivial extrapolation from 2D studies to 3D realistic cases (Jankovic et al., 2016; Zarlenga et al., 2018; Colecchio et al., 2021), particularly regarding percolative properties that strongly depend on dimensionality, we have chosen to work in 3D, despite the high CPU cost.

The paper is structured as follows: In Section 2 we present the numerical methodology, including the generation of media samples, the identification of the percolation threshold of the k^+ facies, and the computation of flow and transport quantities. The results are presented in Section 3, where flow parameters are first addressed, to then focus on the arrival times and dispersivity of the solute, as a function of the connectivity parameters. As we deal with highly heterogeneous media samples, the achievement of an asymptotic regime requires detailed assessment, and is therefore deferred to Appendix A. In Section 4, we discuss our results in a percolation framework, outline the conclusions and examine perspectives for future work.

2. Materials and methods

The procedure consisted of:

- Generation of binary media samples characterized by three parameters: a proportion p of the k^+ facies ($0 < p < 1$), an integral scale I_b (yielding its "grain size"), and a connectivity structure type (no, low, intermediate, high), that controls how well the k^+ facies is connected. Determination of the percolation threshold p_c of the k^+ facies (the value of p for which a cluster of k^+ cells spans the sample along the mean flow direction).
- Computation of the flow velocity field and simulation of solute transport.

These are developed below in detail:

2.1. Generation of binary media samples with different connectivity structure types

The binary media samples are constructed in three steps, as follows:

1. Generation of multigaussian media samples of dimensions $L_x = 2048\Delta, L_y = L_z = 256\Delta$ (the linear size of a cell is $\Delta = 1$ m), using a spectral method through the code FFTW (Gutjahr, 1989; Frigo and Johnson, 2005). Here x is the mean flow direction while y and z are orthogonal to it. We use a standard normal distribution of an intermediate indicator $k_i(\bar{r})$, with isotropic gaussian covariance function (Beaudoin and de Dreuzy, 2013). Due to the very elevated CPU cost associated with the employed media sizes, only two realizations were generated for verification purposes, with good agreement among them.
2. Modification of the connectivity of the multigaussian samples by using a normal score transform (NST) (Zinn and Harvey, 2003) to swap the intermediate $k_i(\bar{r})$ classes with the high (or low) ones. This is performed in four cases depending on the input underlying integral scale I:
   (a) $I \ll \Delta$ (hereafter named I_{ns}, the spatially uncorrelated case used as a reference),
   (b) $I > \Delta$, without applying the NST,
   (c) $I > \Delta$, applying the NST.
   (d) $I > \Delta$, applying the NST, and then multiplying the indicator value $k_i(\bar{r})$ by -1 (i.e. reflecting the indicator values around the mean of their gaussian distribution). For cases $b-c-d$ the studied values of the integral scale I were $1\Delta, 1.5\Delta$ and 2Δ (these are defined after performing the NST, using the gaussian covariance function. We chose these values from a trade-off between the linear size of the grid cell Δ and the length of the samples L_x: On the one hand, as the input parameter I becomes significantly smaller than Δ, it is the latter that controls the actual length-scale of heterogeneity (otherwise said, it does not make sense to study values of I significantly smaller than Δ), while, on the other hand, for values of I significantly greater than 2Δ, it was verified that the asymptotic regime was not achieved even at $x = L_x$. As they are at this stage, the samples will be referred to as underlying media samples.

3. Binarization by standard truncation using a single threshold (Allard, 1993), whose value is determined by the target proportion p of k^+ cells in the binary sample. This procedure maps the $k_i(\bar{r})$ point values (from step 2)) onto $k^+ = 100$ m/day (for the high conductivity facies, in short, the k^+ facies, composed of k^+ cells), or $k^- = 0.01$ m/day (for the low conductivity facies, in short, the k^- facies). Each binary sample has then a proportion p of k^+ cells and a proportion $1-p$ of k^- cells. To enhance our percolative approach, and mimic realistic heterogeneity contrasts, the ratio k^+/k^- was maximized within the possibilities of our CPU resources. The employed contrast of $k^+/k^- = 10^4$ (fixed in this work) is representative of real subsurface systems such as sand-clay ones (Bernabé et al., 2004). The resulting binary samples have one of the following connectivity structures (see 2)):
   (1) No structure.
   (2) Intermediate (a truncated gaussian).
   (3) Low (k^+ cells are preferentially attributed to the underlying disconnected matrix, i.e., they tend to form k^+ isolated blobs embedded in a k^- matrix).
   (4) High (k^+ cells are preferentially attributed to the underlying connected matrix, i.e., they tend to form a k^+ connected network that embeds k^- isolated blobs). Note that cases $b-c-d$ converge to case a if $I = I_{ns}$ (the heterogeneity "texture" becomes uncorrelated noise as I becomes smaller than Δ). The latter is used as a reference to compare with media samples having the same proportion p but lacking any connectivity structure.

Cross sections of the samples obtained with the above procedure are shown in Fig. 1. Binarization maintains the gaussian covariance but modifies the integral scale from I (as of step b) onto I_b (the integral scale of the binary samples), depending on the value of p.

We stress on the following: even when the underlying integral scale I is the parameter initially used to control the heterogeneity lengthscale of the media samples during their generation (steps 1–2), the binarization procedure that follows (step 3) transforms the integral scale from I to I_b, and then, it is indeed the binary integral scale I_b the one that captures the lengthscale the binary samples actually used in the transport simulations.

Note that the outlet face is typically $L_x/I \approx L_x/I_b \approx 2000$ integral scales away from the injection plane (this distance is key to attain the asymptotic regime). This method of generating the binary samples is analogous, yet slightly different, to that reported in Colecchio et al. (2021).

For the high connectivity structure type, k^+ cells tend to form a connected network, while k^- cells tend to form isolated blobs. The opposite occurs for the low connectivity structure type, while the intermediate connectivity structure is simply a truncated gaussian.

The percolation threshold p_c is the lower value of p for which a cluster of k^+ cells (i.e. a k^+ cluster) spans the sample in the mean flow direction. This spanning cluster is composed by the backbone, where flow takes place, and by dead ends. The values of p_c were calculated (for each I and connectivity structure type) using the cluster identification function from the code CONNECT3D (Pardo-Igúzquiza and Dowd, 2003), and are shown in Fig. 2 as a function of the integral scale of the binary media I_b. Face connectivity between cells was considered. The monotonic decrease of p_c with I_b in 3D has already been reported in the literature ((Harter, 2005), Fig. 9 in Colecchio et al. (2021)). Further technical details on the determination of p_c can be found in Colecchio et al. (2021).

2.2. Computation of the flow velocity field and transport quantities

In this study, flow is considered incompressible and non-deformable, then governed by the mass conservation equation coupled with Darcy's law, yielding $\Delta K \Delta h = 0$. An hydraulic head gradient $\Delta h/L_x$ is applied between the inlet and the outlet faces of sample (situated at $x = 0$ and $x = L_x$ respectively), which are orthogonal to the mean flow direction (x axis), while periodic boundary conditions are applied on the long lateral faces (Dartois et al., 2018; Beaudoin et al., 2019). The steady-state flow velocity field $u(x,y,z)$ is solved by using a finite-volume scheme with a uniform regular grid (Chavent and Roberts, 1991), and with harmonic intercell transmissivities (Eymard et al., 2007). With these boundary conditions, $\langle u_y(x,y,z)\rangle_{x,y,z} = \langle u_z(x,y,z)\rangle_{x,y,z} = 0$, while $U_x = \langle u_x(x,y,z)\rangle_{x,y,z}$ is the mean flow velocity. The equivalent conductivity K_{eq} of the sample may be obtained as:

$$K_{eq} = \frac{L_x U_x}{\Delta h} \tag{1}$$

Advection and diffusion of the solute particles are respectively simulated using a first order explicit scheme and a random-walk method, (Rivard and Delay, 2004; Ramirez et al., 2008), the trajectory of the particles being established by a particle-tracking algorithm. A pulse of $N_p = 5000$ particles is injected at $t = 0$ on a plane of size $0.8L_y \times 0.8L_z$, situated perpendicular to the mean flow direction, and 10 I downstream from the inlet face, to avoid border effects (Beaudoin et al., 2019). We use flux proportional particle injection rate (Jankovic et al., 2016) (see Fig. 3).

For clarity, we explain here the computation of the solute mean arrival times and dispersivity, while the assessment of an asymptotic Fickian regime, achieved very far from the injection plane, is deferred to Appendix A. The mean arrival time to the outlet plane is given by Eq. (2) (i labels the particles), which in the Fickian regime coincides with $t_{a50\%}$ the time required for 50% of the particles to reach that plane. We also record $t_{a1\%}$, the time for which 1% of the particles have reached the outlet plane, which is frequently used as a measure of the arrival time of the leading solute plume, and therefore of transport connectivity (Renard and Allard, 2013).

$$\langle t_a \rangle = \frac{\sum_{i=1}^{N_p} t_a^i}{N_p} \tag{2}$$

On the other hand, the longitudinal dispersivity $\alpha_L = D_L/U_x$ is estimated from the time derivative of the second order moment of the particle spatial distribution and from the mean flow velocity U_x (Beaudoin and de Dreuzy, 2013).

Table 1 shows the parameters employed in the simulations.

3. Results

3.1. Mean flow velocities

Fig. 4 shows the variation of the mean flow velocity $U_x = \langle u_x(x,y,z)\rangle_{x,y,z}$, and of K_{eq} (right vertical axis, $K_{eq} \propto U_x$) with the proportion p, for all the studied connectivity parameters. The crosses mark the percolation thresholds p_c from Fig. 2.

For a given value of I, the flow velocities of the high connectivity structure are slightly greater than those of the intermediate one. The no and low connectivity structures may be up to an order of magnitude smaller than the former ones, and show an interesting crossover at $p \approx 0.4 (> p_c)$, for all values of I. This may be due to the fact that, for the low connectivity structure, isolated k^+ blobs become narrowly connected when $p \rightarrow p_c$, giving rise to a backbone with fast flow pathways of very variable cross section (see Fig. 5 f). The characteristic S-shape of the percolation transition (a sharp increase when p approaches p_c, smeared-out by finite size effects and by the finite k^+/k^- contrast) is observed. Aiming to focus on transport more than on flow in this article, we refer to Masihi et al. (2016), and to Colecchio et al. (2021), for detailed discussions on finite size and finite conductivity contrast effects, and on how the variation of K_{eq} (and then of U_x) with p is affected by the connectivity parameters.

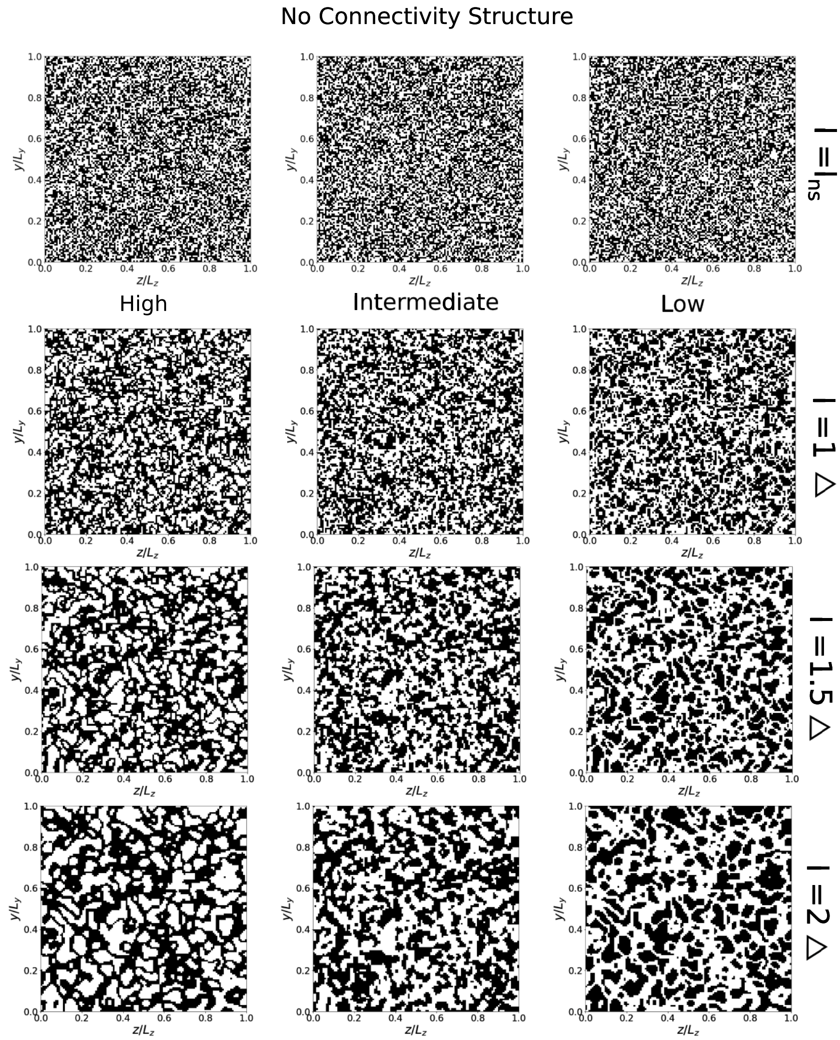

Fig. 1. Cross sections ($y-z$ plane, mean flow is in x−direction) of the 3D binary samples ($L_x = 2048\Delta, L_y = L_z = 256\Delta$) for $p = 0.5$. From top to bottom: $I = I_{ns}$; 1Δ; 1.5Δ and 2Δ. From left to right: high, intermediate and low connectivity structures (■ : $k^+ = 10^2$ m/day, □ : $k^- = 10^{-2}$ m/day). Note that as $I \to I_{ns}$ (i.e. upwards), all connectivity structures converge to the spatially uncorrelated case.

Table 1
Main simulation parameters and units.

Description	Symbol	Representative value(s)	Units
Grid cell linear size	Δ	1	m
Sample linear size	L_x, L_y, L_z	2048 (x); 256 (y, z)	m
Underlying integral scale (as of 2.1)	I	I_{ns}, 1Δ, 1.5Δ; 2Δ	m
Characteristic conductivity of the facies	$k^+(k^-)$	100, (0.01)	m/day
k^+ facies proportion	p	[0, 0.1 … 0.9,]	–
Connectivity structure type	–	No, low, intermediate, high	
Solute molecular diffusion coefficient	D_m	0.01	m^2/day
Hydraulic head gradient	$\Delta h/L_x$	0.01	m/m

3.2. Solute particle distribution: Arrival times $\langle t_a \rangle$, $\langle t_a^* \rangle$

Fig. 6 shows the mean arrival time of the solute particles $\langle t_a \rangle$ as a function of the proportion p for $I = 1.5\Delta$. It decreases monotonically as U_x increases, but more rapidly for the high and intermediate connectivity structures, which behave similarly. The crossover for $p \approx 0.4$, between the no and low connectivity structure, reflects that of Fig. 5.

The crosses indicate the percolation thresholds $p = p_c$ from Fig. 2. The results shown in Fig. 4 reflect those in Fig. 5, greater mean flow velocities U implying smaller arrival times $\langle t_a \rangle$. To assess the explicit effect of the connectivity structure on $\langle t_a \rangle$ we show in Fig. 7 the variation of a dimensionless arrival time $\langle t_a^* \rangle = \frac{\langle t_a \rangle}{\langle t_a \rangle_{ns}}$ with p (here the subscript "ns" stands for "no structure"): this representation makes it possible to decouple the influence on $\langle t_a \rangle$ of the variation of connectivity due to a variation of p from that due to a change in the spatial organization of the k^+ facies. In that figure, $\langle t_a^* \rangle$ has a minimum for p somewhat greater than p_c, its value being almost two orders of magnitude smaller than unity for the high and intermediate connectivity structures. On the other hand, for the low connectivity structure, a minimum also appears just after p_c, but then, $\langle t_a^* \rangle$ increases beyond unity. This shows how the consolidation of flow pathways for $p > p_c$ may imply a strong decrease (what one may expect if channeling exists) but also relative increase of $\langle t_a^* \rangle$, depending on the connectivity structure. We remark a feature that will reappear in the following: in all cases, the minimum of $\langle t_a^* \rangle$ occurs for p somewhat greater than p_c.

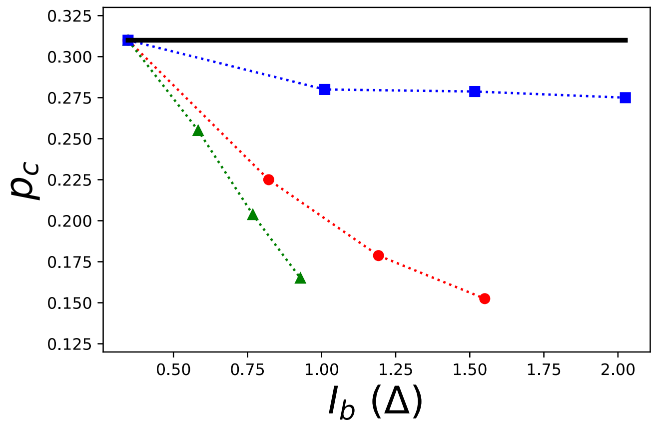

Fig. 2. Percolation thresholds p_c as a function of the binary integral scale I_b for the high (▲), intermediate (●) and low (■) connectivity structure types. (▬): no structure (spatially uncorrelated, $I = I_{ns}$). The limiting value of $p_c = 0.311$ corresponds to site percolation in a cubic regular grid (Stauffer and Aharony, 1994). For each curve, the 1st to 4th datapoints from left to right correspond to $I = I_{ns}$; 1Δ; 1.5Δ and 2Δ respectively. The dotted lines are guides to the eye.

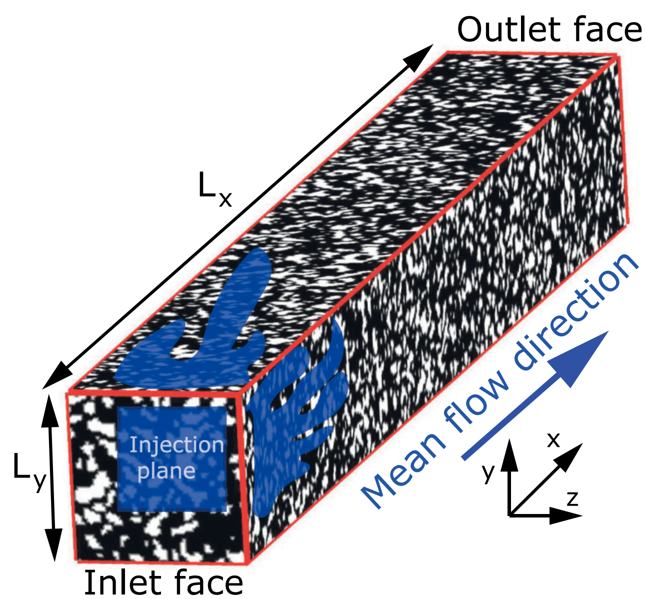

Fig. 3. Scheme (perspective view) of the computational domain and flow conditions employed in this work to study the transport of a solute. The 3D media sample shown has a high connectivity structure with $p = 0.4$ and $I = 1.5\Delta$. (■ : $k^+ = 10^2$ m/day, □ : $k^- = 10^{-2}$ m/day). An hydraulic head gradient Δh is applied between the inlet and the outlet faces of the sample (situated at $x = 0$ and $x = L_x$), while periodic boundary conditions are applied on the lateral faces of the sample. The solute particles are injected on a plane of size $0.8L_y \times 0.8L_z$ situated at 10 I downstream from the inlet face.

3.3. Solute particle distribution: Longitudinal dispersivity α_L

Very long media samples were used so that an asymptotic Fickian regime could be attained far from the injection plane, despite the high degree of heterogeneity of the studied samples : This is assessed in detail in the A, where we also show that the longitudinal solute dispersivity α_L is well-defined in the asymptotic regime. In the following, we only address this regime. The dispersivity α_L is shown in Fig. 8, as a function of p.

The mechanism of dispersion results from molecular diffusion, and from the spatial variability of the flow velocity field occurring at all scales (pore to formation) (Frippiat and Holeyman, 2008; Gelhar et al., 1992). In the case of 3D binary media considered here, if p approaches the extreme values 0 or 1, these 3D binary media become homogeneous media, respectively with $K_{eq} = K^-$ or K^+. Thus the spatial variations of the flow velocity field vanish, and dispersivity α_L is only driven by molecular diffusion. In between, the inhomogeneities of the flow field give rise to mechanical dispersion. Notably, for all the combinations of connectivity parameters studied, the rate of increase of α_L with p is maximal at $p = p_c$ (note that p_c varies with the connectivity structure type and with I, as shown in Fig. 2), while α_L itself shows a maximum for p slightly greater than p_c (reflecting the minima of Fig. 7). Also, the peak value of α_L for the low connectivity structure type nearly duplicates that for the high one (and it is an order of magnitude greater than that of the no structure case). These results are discussed in detail in the next section.

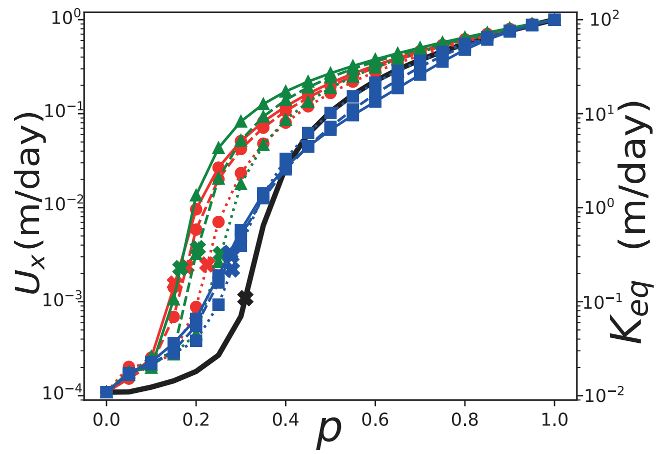

Fig. 4. Mean flow velocity $U_x = \langle u_x(x,y,z)\rangle_{x,y,z}$ (left vertical axis) and equivalent conductivity K_{eq} (right vertical axis) as a function of p for the high (▲), intermediate (●) and low (■) connectivity structure types. (▬): no structure (spatially uncorrelated, $I = I_{ns}$); (⋯⋯): $I = 1\Delta$; (‒ ‒ ‒): $I = 1.5\Delta$; and (——): $I = 2\Delta$. The crosses indicate the percolation threshold p_c from Fig. 2.

4. Discussion and conclusions

We provide here, for clarity, our interpretation of how flow and transport evolve as p increases, in particular, as the percolation transition occurs. Fig. 5 shows a conceptual scheme of this transition.

1. For $p \approx 0$, $k(\bar{r}) = k^- \forall \bar{r}$, $K_{eq} = k^-$, the flow velocity field is homogeneous, and the dispersivity of the solute is only driven by molecular diffusion.
2. For $0 < p < 0.15 < p_c$, U_x (and then K_{eq}) slowly increases with p, the local flow velocities show mild spatial fluctuations, the variance of solute particle velocities also slowly increases with p (Fig. 5 a, c, e)
3. Eventually, as p reaches p_c, a spanning cluster of k^+ cells appears, connecting the inlet and outlet faces of the sample. This cluster is composed by a backbone (at this point made of very narrow channels), where significant flow takes place, and by dead ends with no flow. A small fraction of the solute particles now suddenly sample very high flow velocities within the fast flow pathways of the backbone, U_x shows a sharp increase and then $\langle t_a \rangle$ a sharp decrease. On the other hand, a large fraction of particles sample low flow velocities outside the backbone. This implies an important increase of the variance of solute particle velocities, and then of dispersivity, which is observed in Fig. 8.
4. As p departs from p_c, the volume fraction of the backbone (now made of broader consolidated channels) increases, the minima of $\langle t_a \rangle$ in Fig. 7 and the maxima of α_L in Fig. 8 take place. Now a moderate fraction of solute particles sample high velocities

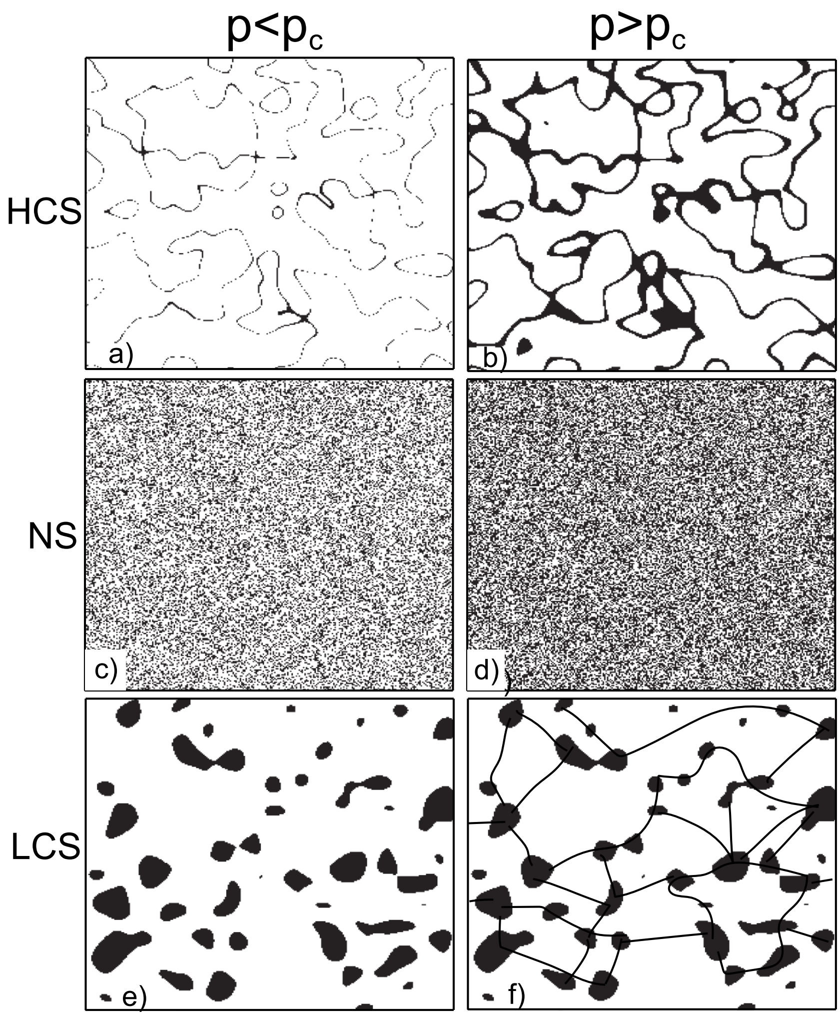

Fig. 5. Conceptual scheme of the onset of percolation in the high (a, b), no (c, d) and low (e, f) connectivity structures (■ : k^+; □ : k^-), for the range $0.15 < p < 0.3$ at which percolation occurs in 3D (see. Fig. 2). For the high one (a, b), a connected network of k^+ cells consolidates as p exceeds p_c $(a \rightarrow b)$, making for fast flow pathways within the backbone. Note that these have a rather homogeneous cross section (b). For the low one, isolated k^+ blobs get connected as $p \rightarrow p_c$ $(e \rightarrow f)$. Because p_c is much higher in 2D than in 3D (Stauffer and Aharony, 1994), the spanning cluster is not visible in f), so it is represented by joining the k^+ blobs by narrow links. In $c - d$, the no structure case is shown as a reference.

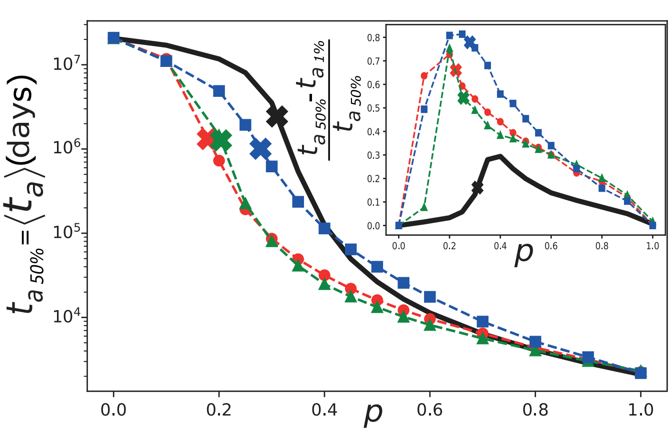

Fig. 6. Mean arrival time of the solute particles as a function of p for the high (▲), intermediate (●) and low (■) connectivity structure types and $I = 1.5\Delta$. (▬): the no structure case (spatially uncorrelated, $I = I_{ns}$). The crosses indicate the percolation thresholds $p = p_c$ from Fig. 2. The high and intermediate connectivity structures behave similarly, while the no and low connectivity structure types show relatively much greater values of $\langle t_a \rangle$, while the crossover of Fig. 4 can be observed. Inset shows $\frac{t_{a50\%} - t_{a1\%}}{t_{a50\%}}$, a measure of the width of the distribution of t_a relative to $\langle t_a \rangle$.

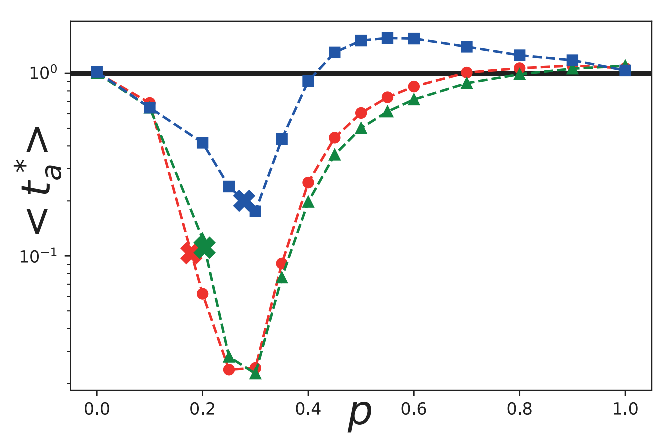

Fig. 7. Normalized mean arrival times $\langle t_a^* \rangle = \langle t_a \rangle / \langle t_a \rangle_{ns}$ as a function of p, for the high (▲), intermediate (●) and low (■) connectivity structure types and $I = 1.5\Delta$. An inverted peak (a minimum) exists for $0.2 < p < 0.3$. The crosses indicate the percolation threshold $p = p_c$, while the dotted line indicates unity.

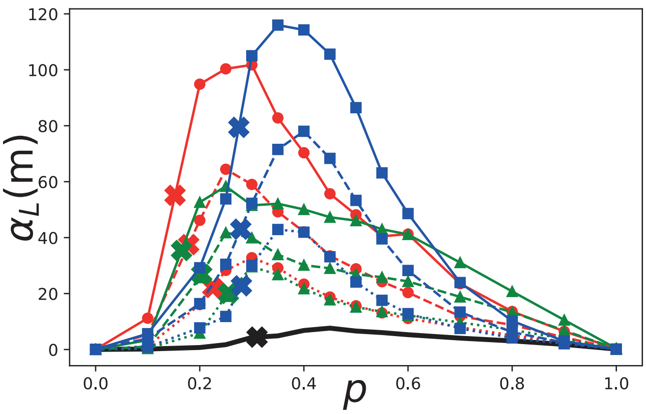

Fig. 8. Dispersivity α_L as a function of the proportion p for the high (▲), intermediate (●) and low (■) connectivity structure types. (▬): the no structure case (spatially uncorrelated, $I = I_{ns}$), (····): $I = 1\Delta$, (– – –): $I = 1.5\Delta$ and (—): $I = 2\Delta$. Crosses indicate $p = p_c$, where, notably, the maximum rate of increase of α_L with p takes place, preceding its peak. In all cases, α_L increases with I for fixed connectivity structure and p.

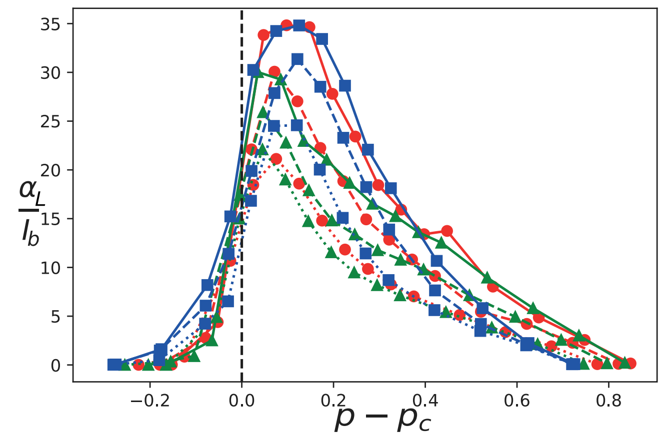

Fig. 9. Data collapse: Dispersivity α_L normalized by the binary integral scale I_b as a function of $p - p_c$ for the high (▲), intermediate (●) and low (■) connectivity structure types. (····): $I = 1\Delta$, (– – –): $I = 1.5\Delta$ and (—): $I = 2\Delta$.

within the fast flow pathways of the backbone. For the low connectivity structure, the backbone is composed of k^+ blobs connected by narrow k^+ links (Fig. 5 f), giving rise to flow pathways of very variable cross section, and possibly to solute retention or trapping. On the other hand, for the high connectivity structure (Fig. 5 b), a connected network fast flow pathways, of rather uniform cross section, becomes consolidated.

5. Finally, as p approaches unity, $k(\bar{r}) \rightarrow k^+ \forall \bar{r}$ ($K_{eq} = k^+$), the flow spatial inhomogeneities disappear, the variance of particle velocities vanishes, and the dispersivity of the solute is driven again only by molecular diffusion, in symmetry with (a).

The occurrence of D_L maximum for $p \sim p_c$ has already been reported in 2D percolation networks by Rivard and Delay (2004). In Fig. 6 from that work, it can be clearly observed that this maximum occurs for $p > p_c$. As the authors state, at $p = p_c$ very few solute particles can only sample the high velocities within the narrow and tortuous backbone, and they do so for very short time lapses (arrival times are comparable to those for $p < p_c$). It is required that p exceeds p_c so that broader k^+ channels, and then broader fast flow pathways, consolidate (Fig. 5 b, d, f), and so that a significant fraction of particles can sample velocities within them, with the consequent increase of particle velocity variances and then of α_L.

One may wonder if the passage from the steep increase of α_L at $p = p_c$ to the subsequent maximum for $p > p_c$, observed in Fig. 8, occurs in a similar manner for the different connectivity parameters. Also, in the same figure, it is observed that, I kept fixed, the low connectivity structure is the most dispersive one, and that the peak value of α_L for that structure nearly duplicates that of the high one (with the intermediate in between).

To clarify both issues, we show in Fig. 9 the normalized dispersivity α_L/I_b as a function of $p - p_c$, where I_b is the binary integral scale shown in Fig. 2. The horizontal collapse is rather satisfactory, showing more clearly that the onset of percolation systematically triggers a steep increase and a subsequent maximum of α_L, and the peaks for all the combinations of connectivity parameters take place in the short range $0 < p - p_c < 0.1$. This suggests that the influence of the connectivity parameters on these features of the α_L dependence on p is exerted mainly through a shift in the percolation threshold p_c, with some analogy with a result obtained by Colecchio et al. (2021) for K_{eq}.

Also, vertically wise, in this representation the ratio of two between maxima is reduced from 2 to 1.4, implying that I_b controls in some measure the magnitude of α_L, but an explicit dependence on the connectivity structure type exists beyond the influence of I_b. Probably, the use of I_b to scale α_L could be greatly improved by the use of a non-cartesian length metrics such as the ones described in Renard and Allard (2013). We have tested some, such as the percolation correlation length ξ and the connectivity function $\tau(\bar{r})$, without any clear findings. Notably, the high connectivity structure remains the least dispersive even when the effect of its smaller I_b has been corrected.

In that regard, Fiori et al. (2010) studied transport continuous media for which the integral scale I was not constant, but defined as a function of $\ln(k(\bar{r}))$. These authors found a decrease of the asymptotic dispersivity when the high $k(\bar{r})$ values were more spatially correlated, due to solute trapping in the low $k(\bar{r})$ zones, which is in agreement with our results. On the other hand, Zarlenga and Fiori (2015) found an increase of dispersion when the high $k(\bar{r})$ values formed a connected matrix in bimodal media, as the low $k(\bar{r})$ non-overlapping inclusions retained the solute particles. This is somehow in contrast with our results, for which the high connectivity structure is the least dispersive. We recall that previous authors reported a clear dependence of the solute BTC's on the connectivity structure type in 2D lognormal fields (Zinn and Harvey, 2003), but, in 3D, simulations of showed BTC curves that were "practically independent" of the connectivity structure, even when a wide variety of them were considered (Jankovic et al., 2016). Our results show that this independence does not hold for highly heterogeneous binary media. On the contrary, we observe that transport quantities still retain the signature of the connectivity features sampled by the solute particles during their trajectories even after the Fickian regime is attained. Even though the connectivity structures addressed in this work span, to some extent and within the studied range of parameters, the best (high connectivity structure) and worst (low connectivity structure)-case scenarios of connectivity, we recall that the studied media samples constitute a very simplistic view of natural geological media, which typically show much more complex heterogeneity and connectivity features. Determining connectivity in real sites requires extensive characterization through a wide variety of methods, which often need to take into account higher order statistics. This characterization is a difficult task due to few available data. Also, in this work we only consider transport under ergodic conditions, while non-ergodic conditions may be found in many applications. In that case, a proper uncertainty analysis would be required to determine the transport quantities. Finally, we understand that further research should be also conducted to characterize thoroughly the very interesting region between the occurrence of percolation ($p = p_c$) and peak of dispersivity that follows as p increases. This region could be studied in more detail by analyzing the probability density function of particle velocities.

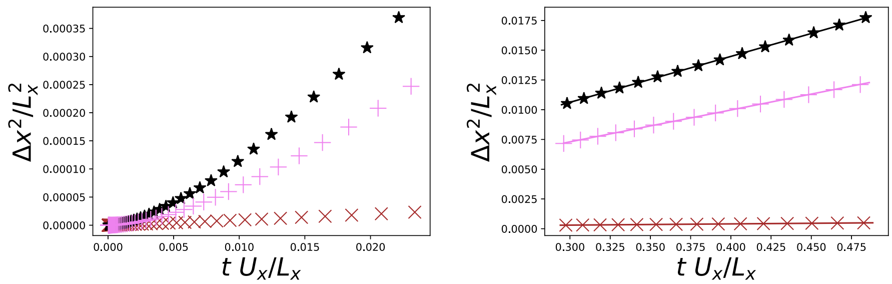

Fig. A.1. The second moment of the normalized solute particle spatial distribution $\Delta x^2/L_x^2$ as a function of the dimensionless time $t\ U_x/L_x$, for the high connectivity structure and for: (×) $p = 0.1$, (★) $p = 0.3$ and (+) $p = 0.5$. Left: Early times, for which the solute particle cloud is near the injection plane. Right: Late times, for which the cloud is far from the injection plane, but all particles are still within the sample. The solid line is a linear fit. Note that U_x is a function of p (see Fig. 4).

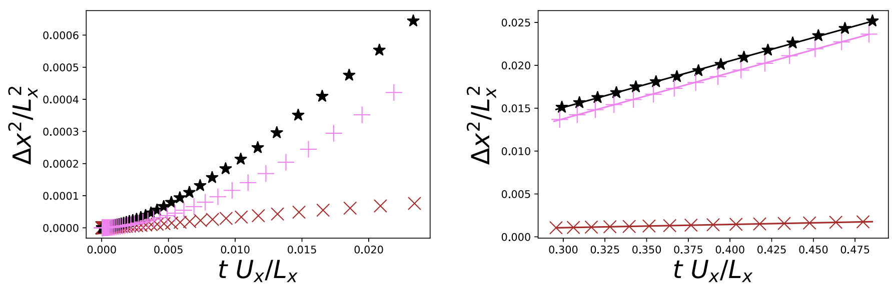

Fig. A.2. The second moment of the normalized solute particle spatial distribution $\Delta x^2/L_x^2$ as a function of the dimensionless time $t\ U_x/L_x$, for the low connectivity structure and for: (×) $p = 0.1$, (★) $p = 0.3$ and (+) $p = 0.5$. Left: Early times, for which the solute particle cloud is near the injection plane. Right: Late times, for which the cloud is far from the injection plane, but all particles are still within the sample. The solid line is a linear fit.

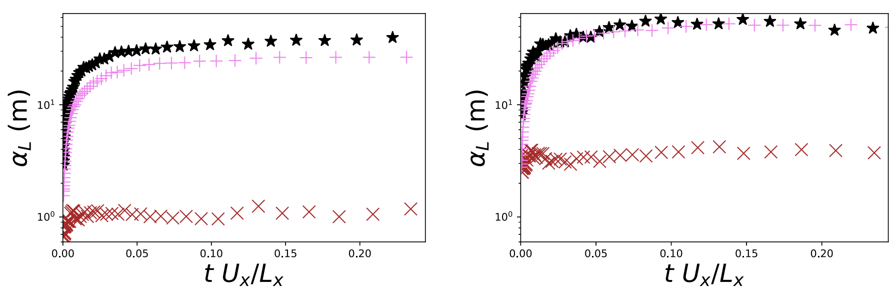

Fig. A.3. Dispersivity α_L as a function of the dimensionless time $t\ U_x/L_x$ for the high (left) and low (right) connectivity structure types. For both $I = 1.5\Delta$ and (×) $p = 0.1$, (★) $p = 0.3$ and (+) $p = 0.5$.

CRediT authorship contribution statement

Anthony Beaudoin: Conceptualization, Methodology, Software, Writing – review & editing. **Iván Colecchio:** Conceptualization, Methodology, Software, Writing – review & editing. **Alejandro Boschan:** Conceptualization, Methodology, Software, Writing – review & editing.

Declaration of competing interest

The authors declare that they have no known competing financial interests or personal relationships that could have appeared to influence the work reported in this paper.

Data availability

Data will be made available on request.

Funding sources

1) Université de Poitiers
2) IRP CNRS-CONICET Ingénieries vertes par la mécanique des fluides

Appendix A. Achievement of the asymptotic Fickian regime

Here the achievement of an asymptotic Fickian regime very far from the injection plane is assessed. We recall that this regime can only be obtained in our simulations due to the use of very long media samples, i.e, using monitoring positions situated at $x/I \approx x/I_b \approx 2000$ (i.e. 2000 integral scales away from the injection plane), while previous works typically reported much closer monitoring distances (e.g. 63 integral scales away (Jankovic et al., 2016). Fig. A.1 shows the early (left) and late (right) dependence of the second moment of the solute particle spatial distribution $\Delta x^2 = \langle x_i^2(t)\rangle - \langle x_i(t)\rangle^2\rangle$, (here the index i labels the particles) normalized by the squared sample length L_x^2, with the dimensionless time tU_x/L_x, for $p = 0.1$; 0.3; 0.5 (i.e. taking into account both sides of the percolation transition), for $I = 1.5\Delta$, and for the high connectivity structure. Fig. A.2 shows the same, but for the low connectivity structure. For both, at early times, the non-linear variation implies a non-Fickian regime, while, for late times, the linear variation implies a diffusive Fickian one, with a well-defined longitudinal dispersivity. The linear regressions yield $R^2 > 0.99$ for all late time behaviors. Note that U_x is a function of p (see Fig. 4).

The characteristic diffusion time is $\tau_D \approx I_b^2/D_m \approx 100$ days. If we require it to be 10 times smaller than the characteristic advective time $\tau_A \approx L_x/U_x$, then, considering $U_x = 1$ m/s as an upper bound, the

Fickian regime is typically attained at $x \approx 1000$ m, i.e. half way of the sample length.

Fig. A.3 shows how α_L attains its asymptotic value very far from the injection plane.

References

Allard, D., 1993. On the connectivity of two random set models: The truncated Gaussian and the Boolean. Quant. Geolo. Geostat. 5, 467–478. http://dx.doi.org/10.1007/978-94-011-1739-5_37.

Beaudoin, A., Dartois, A., Huberson, S., 2019. Analysis of the influence of averaged positive second invariant Q of deformation tensor ∇ u on the maximum dilution index E in steady Darcy flows through isotropic heterogeneous porous media. Adv. Water Resour. 128, http://dx.doi.org/10.1016/j.advwatres.2019.03.008.

Beaudoin, A., de Dreuzy, J.-R., 2013. Numerical assessment of 3-D macrodispersion in heterogeneous porous media. Water Resour. Res. 49 (5), 2489–2496. http://dx.doi.org/10.1002/wrcr.20206, arXiv:https://agupubs.onlinelibrary.wiley.com/doi/pdf/10.1002/wrcr.20206.

Ben-Noah, I., Hidalgo, J.J., Jimenez-Martinez, J., Dentz, M., 2023. Solute trapping and the mechanisms of non-Fickian transport in partially saturated porous media. Water Resour. Res. 59 (2), http://dx.doi.org/10.1029/2022WR033613, arXiv:https://agupubs.onlinelibrary.wiley.com/doi/pdf/10.1029/2022WR033613. e2022WR033613 2022WR033613.

Berkowitz, B., Scher, H., 1995. On characterization of anomalous dispersion in porous and fractured media. Water Res Res - WATER RESOUR RES 31, 1461–1466. http://dx.doi.org/10.1029/95WR00483.

Berkowitz, B., Scher, H., 1997. Anomalous transport in random fracture networks. Phys. Rev. Lett. 79, 4038–4041. http://dx.doi.org/10.1103/PhysRevLett.79.4038, URL https://link.aps.org/doi/10.1103/PhysRevLett.79.4038.

Bernabé, Y., Mok, U., Evans, B., Herrmann, F., 2004. Permeability and storativity of binary mixtures of high- and low-permeability materials. J. Geophys. Res.: Solid Earth 109 (B12), http://dx.doi.org/10.1029/2004JB003111.

Bianchi, M., Palamakumbura, R., Macdonald, A., Macdonald, D., 2023. Assessing regional variation in yield from weathered basement aquifers in west Africa and modelling their future groundwater development and sustainability. Hydrogeol. J. http://dx.doi.org/10.1007/s10040-023-02594-w.

Bianchi, M., Zheng, C., 2016. A lithofacies approach for modeling non-fickian solute transport in a heterogeneous alluvial aquifer. Water Resour. Res. 52 (1), 552–565. http://dx.doi.org/10.1002/2015WR018186, arXiv:https://agupubs.onlinelibrary.wiley.com/doi/pdf/10.1002/2015WR018186.

Boschan, A., Noetinger, B., 2012. Scale dependence of effective hydraulic conductivity distributions in 3D heterogeneous media: A numerical study. Transp. Porous Media 94 (1), 101–121. http://dx.doi.org/10.1007/s11242-012-9991-2.

Bradley, J., Singh, K., Wang, L., 2023. Intrapore geometry and flow rate controls on the transition of non-Fickian to Fickian dispersion. Water Resour. Res. 59 (1), http://dx.doi.org/10.1029/2022WR032833, e2022WR032833.

Chavent, G., Roberts, J., 1991. A unified physical presentation of mixed, mixed-hybrid finite elements and standard finite difference approximations for the determination of velocities in waterflow problems. Adv. Water Resour. 14 (6), 329–348. http://dx.doi.org/10.1016/0309-1708(91)90020-O, URL https://www.sciencedirect.com/science/article/pii/030917089190020O.

Cirpka, O.A., Stettler, M.-M., Dentz, M., 2022. Spatial Markov model for the prediction of travel-time-based solute dispersion in three-dimensional heterogeneous media. Water Resour. Res. 58 (6), http://dx.doi.org/10.1029/2022WR032215, e2022WR032215.

Colecchio, I., Otero, A.D., Noetinger, B., Boschan, A., 2021. Equivalent hydraulic conductivity, connectivity and percolation in 2D and 3D random binary media. Adv. Water Resour. 158, 104040. http://dx.doi.org/10.1016/j.advwatres.2021.104040, URL https://www.sciencedirect.com/science/article/pii/S0309170821001949.

Dagan, G., 1989. Flow and Transport in Porous Formations. Springer-Verlag GmbH & Co. KG., http://dx.doi.org/10.1007/978-3-642-75015-1.

Dartois, A., Beaudoin, A., Huberson, S., 2018. Impact of local diffusion on macroscopic dispersion in three-dimensional porous media. Comptes Rendus Mécanique 346 (2), 89–97. http://dx.doi.org/10.1016/j.crme.2017.12.012, URL https://www.sciencedirect.com/science/article/pii/S1631072117302395.

De Caro, M., Perico, R., Crosta, G.B., Frattini, P., Volpi, G., 2020. A regional-scale conceptual and numerical groundwater flow model in fluvio-glacial sediments for the Milan metropolitan area (northern Italy). J. Hydrol.: Reg. Stud. 29, 100683. http://dx.doi.org/10.1016/j.ejrh.2020.100683, URL https://www.sciencedirect.com/science/article/pii/S2214581819302058.

de Dreuzy, J.-R., Beaudoin, A., Erhel, J., 2007. Asymptotic dispersion in 2D heterogeneous porous media determined by parallel numerical simulations. Water Resour. Res. 43, http://dx.doi.org/10.1029/2006WR005394.

Dentz, M., Lester, D.R., Speetjens, M.F., 2023. Editorial to the special issue: Mixing in porous media. Transp. Porous Media http://dx.doi.org/10.1007/s11242-022-01899-w, URL https://api.elsevier.com/content/abstract/scopus_id/85145852462.

Edery, Y., Guadagnini, A., Scher, H., Berkowitz, B., 2014. Origins of anomalous transport in heterogeneous media: Structural and dynamic controls. Water Resour. Res. 50 (2), 1490–1505. http://dx.doi.org/10.1002/2013WR015111, arXiv:https://agupubs.onlinelibrary.wiley.com/doi/pdf/10.1002/2013WR015111.

Eymard, R., Gallouët, T., Herbin, R., 2007. A new finite volume scheme for anisotropic diffusion problems on general grids: Convergence analysis. C. R. Math. 344 (6), 403–406. http://dx.doi.org/10.1016/j.crma.2007.01.024, URL https://www.sciencedirect.com/science/article/pii/S1631073X07000465.

Fiori, A., Boso, F., de Barros, F., De Bartolo, S., Frampton, A., Severino, G., Suweis, S., Dagan, G., 2010. An indirect assessment on the impact of connectivity of conductivity classes upon longitudinal asymptotic macrodispersivity. Water Resour. Res. 46, http://dx.doi.org/10.1029/2009WR008590.

Fiori, A., Zarlenga, A., Jankovic, I., Dagan, G., 2017. Solute transport in aquifers: The comeback of the advection dispersion equation and the first order approximation. Adv. Water Resour. 110, 349–359. http://dx.doi.org/10.1016/j.advwatres.2017.10.025, URL https://www.sciencedirect.com/science/article/pii/S030917081730177X.

Fleckenstein, J., Fogg, G., 2008. Efficient upscaling of hydraulic conductivity in heterogeneous alluvial aquifers. Hydrogeol. J. 16, 1239–1250. http://dx.doi.org/10.1007/s10040-008-0312-3.

Fogg, G.E., 1986. Groundwater flow and sand body interconnectedness in a thick, multiple-aquifer system. Water Resour. Res. 22 (5), 679–694. http://dx.doi.org/10.1029/WR022i005p00679, arXiv:https://agupubs.onlinelibrary.wiley.com/doi/pdf/10.1029/WR022i005p00679.

Freeze, R.A., 1975. A stochastic-conceptual analysis of one-dimensional groundwater flow in nonuniform homogeneous media. Water Resour. Res. 11 (5), 725–741. http://dx.doi.org/10.1029/WR011i005p00725, URL https://agupubs.onlinelibrary.wiley.com/doi/abs/10.1029/WR011i005p00725.

Frigo, M., Johnson, S., 2005. The design and implementation of FFTW3. Proc. IEEE 93 (2), 216–231. http://dx.doi.org/10.1109/JPROC.2004.840301.

Frippiat, C., Holeyman, A., 2008. A comparative review of upscaling methods for solute transport in heterogeneous porous media. J. Hydrol. 362, 150–176. http://dx.doi.org/10.1016/j.jhydrol.2008.08.015.

Gelhar, L.W., 1986. Stochastic subsurface hydrology from theory to applications. Water Resour. Res. 22 (9S), 135S–145S. http://dx.doi.org/10.1002/9781118782088.ch12.

Gelhar, L.W., Welty, C., Rehfeldt, K.R., 1992. A critical review of data on field-scale dispersion in aquifers. Water Resour. Res. 28 (7), 1955–1974. http://dx.doi.org/10.1029/92WR00607, arXiv:https://agupubs.onlinelibrary.wiley.com/doi/pdf/10.1029/92WR00607.

Gouze, P., Le Borgne, T., Leprovost, R., Lods, G., Poidras, T., Pezard, P., 2008. Non-fickian dispersion in porous media: 1. Multiscale measurements using single-well injection withdrawal tracer tests. Water Resour. Res. 44 (6), http://dx.doi.org/10.1029/2007WR006278, arXiv:https://agupubs.onlinelibrary.wiley.com/doi/pdf/10.1029/2007WR006278.

Guin, A., Ritzi, Jr., R.W., 2008. Studying the effect of correlation and finite-domain size on spatial continuity of permeable sediments. Geophys. Res. Lett. 35 (10), http://dx.doi.org/10.1029/2007GL032717.

Gutjahr, A., 1989. Fast Fourier Transforms for Random Field Generation: Project Report for Los Alamos Grant to New Mexico Tech. New Mexico Institute of Mining and Technology, URL https://books.google.com.ar/books?id=qhUcHAAACAAJ.

Harter, T., 2005. Finite-size scaling analysis of percolation in three-dimensional correlated binary Markov chain random fields. Phys. Rev. E 72, 026120. http://dx.doi.org/10.1103/PhysRevE.72.026120.

Huang, C., Dai, Z., 2008. Modeling groundwater in multimodal porous media with localized decompositions. Math. Geosci. 40 (6), 16.

Jankovic, I., Fiori, A., Dagan, G., 2006. Modeling flow and transport in highly heterogeneous three-dimensional aquifers: Ergodicity, Gaussianity, and anomalous behavior—1. Conceptual issues and numerical simulations. Water Res. Res. - WATER RESOUR RES 420, http://dx.doi.org/10.1029/2005WR004734.

Jankovic, I., Maghrebi, M., Fiori, A., Dagan, G., 2016. When good statistical models of aquifer heterogeneity go right: The impact of aquifer permeability structures on 3D flow and transport. Adv. Water Resour. 100, 199–211. http://dx.doi.org/10.1016/j.advwatres.2016.10.024.

Journel, A., Alabert, F., 1989. Non-Gaussian data expansion in the earth sciences. Terra Nova 1 (2), 123–134. http://dx.doi.org/10.1111/j.1365-3121.1989.tb00344.x, arXiv:https://onlinelibrary.wiley.com/doi/pdf/10.1111/j.1365-3121.1989.tb00344.x.

Knudby, C., Carrera, J., Bumgardner, J.D., Fogg, G.E., 2006. Binary upscaling the role of connectivity and a new formula. Adv. Water Resour. 29 (4), 590–604. http://dx.doi.org/10.1016/j.advwatres.2005.07.002.

Kong, X.-Z., Ahkami, M., Naets, I., Saar, M.O., 2023. The role of high-permeability inclusion on solute transport in a 3D-printed fractured porous medium: An LIF-PIV integrated study. Transp. Porous Media 1 (283), 305. http://dx.doi.org/10.3929/ethz-b-000561090.

Koplik, J., Redner, S., Wilkinson, D., 1988. Transport and dispersion in random networks with percolation disorder. Phys. Rev. A 37, 2619–2636. http://dx.doi.org/10.1103/PhysRevA.37.2619, URL https://link.aps.org/doi/10.1103/PhysRevA.37.2619.

Le Borgne, T., Dentz, M., Davy, P., Bolster, D., Carrera, J., de Dreuzy, J.-R., Bour, O., 2011. Persistence of incomplete mixing: A key to anomalous transport. Phys. Rev. E 84, 015301. http://dx.doi.org/10.1103/PhysRevE.84.015301, URL https://link.aps.org/doi/10.1103/PhysRevE.84.015301.

Lester, D.R., Dentz, M., Singh, P., Bandopadhyay, A., 2023. Under what conditions does transverse macrodispersion exist in groundwater flow? Water Resour. Res. 59 (3), http://dx.doi.org/10.1029/2022WR033059, e2022WR033059.

Masihi, M., Gago, P., King, P., 2016. Estimation of the effective permeability of heterogeneous porous media by using percolation concepts. Transp. Porous Media 114, http://dx.doi.org/10.1007/s11242-016-0732-9.

Matheron, G., De Marsily, G., 1980. Is transport in porous media always diffusive? A counterexample. Water Resour. Res. 16 (5), 901–917. http://dx.doi.org/10.1029/WR016i005p00901, arXiv:https://agupubs.onlinelibrary.wiley.com/doi/pdf/10.1029/WR016i005p00901.

McKenna, S.A., Ray, J., Marzouk, Y., van Bloemen Waanders, B., 2011. Truncated multiGaussian fields and effective conductance of binary media. Adv. Water Resour. 34 (5), 617–626. http://dx.doi.org/10.1016/j.advwatres.2011.02.011, URL https://www.sciencedirect.com/science/article/pii/S0309170811000376.

Molinari, A., Guadagnini, L., Marcaccio, M., Guadagnini, A., 2019. Geostatistical multimodel approach for the assessment of the spatial distribution of natural background concentrations in large-scale groundwater bodies. Water Res. 149, 522–532. http://dx.doi.org/10.1016/j.watres.2018.09.049, URL https://www.sciencedirect.com/science/article/pii/S0043135418307644.

Moroni, M., Kleinfelter, N., Cushman, J.H., 2007. Analysis of dispersion in porous media via matched-index particle tracking velocimetry experiments. Adv. Water Resour. 30 (1), 1–15. http://dx.doi.org/10.1016/j.advwatres.2006.02.005, URL https://www.sciencedirect.com/science/article/pii/S0309170806000388.

Oriani, F., Renard, P., 2014. Binary upscaling on complex heterogeneities: The role of geometry and connectivity. Adv. Water Resour. 64, 47–61. http://dx.doi.org/10.1016/J.ADVWATRES.2013.12.003.

Pardo-Igúzquiza, E., Dowd, P.A., 2003. CONNEC3D: A computer program for connectivity analysis of 3D random set models. Comput. Geosci. 29 (6), 775–785. http://dx.doi.org/10.1016/S0098-3004(03)00028-1.

Poeter, E., Townsend, P., 1994. Assessment of critical flow path for improved remediation management. Groundwater 32 (3), 439–447. http://dx.doi.org/10.1111/j.1745-6584.1994.tb00661.x, arXiv:https://ngwa.onlinelibrary.wiley.com/doi/pdf/10.1111/j.1745-6584.1994.tb00661.x.

Ramirez, J.M., Thomann, E.A., Waymire, E.C., Chastanet, J., Wood, B.D., 2008. A note on the theoretical foundations of particle tracking methods in heterogeneous porous media. Water Resour. Res. 44 (1), http://dx.doi.org/10.1029/2007WR005914.

Renard, P., Allard, D., 2013. Connectivity metrics for subsurface flow and transport. Adv. Water Resour. 51, 168–196. http://dx.doi.org/10.1016/j.advwatres.2011.12.001, 35th Year Anniversary Issue.

Rivard, C., Delay, F., 2004. Simulations of solute transport in fractured porous media using 2D percolation networks with uncorrelated hydraulic conductivity fields. Hydrogeol. J. 12, 613–627. http://dx.doi.org/10.1007/s10040-004-0363-z.

Rizzo, C.B., de Barros, F.P.J., 2017. Minimum hydraulic resistance and least resistance path in heterogeneous porous media. Water Resour. Res. 53 (10), 8596–8613. http://dx.doi.org/10.1002/2017WR020418, arXiv:https://agupubs.onlinelibrary.wiley.com/doi/pdf/10.1002/2017WR020418.

Rizzo, C.B., de Barros, F.P.J., 2019. Minimum hydraulic resistance uncertainty and the development of a connectivity-based iterative sampling strategy. Water Resour. Res. 55 (7), 5593–5611. http://dx.doi.org/10.1029/2019WR025269, arXiv:https://agupubs.onlinelibrary.wiley.com/doi/pdf/10.1029/2019WR025269.

Rubin, Y., 1995. Flow and transport in bimodal heterogeneous formations. Water Resour. Res. 31 (10), 2461–2468. http://dx.doi.org/10.1029/95WR01953, arXiv:https://agupubs.onlinelibrary.wiley.com/doi/pdf/10.1029/95WR01953.

Sahimi, M., 1987. Hydrodynamic dispersion near the percolation threshold: Scaling and probability densities. J. Phys. A: Math. Gen. 20 (18), L1293. http://dx.doi.org/10.1088/0305-4470/20/18/013.

Sahimi, M., 2012. Dispersion in porous media, continuous-time random walks, and percolation. Phys. Rev. E 85, 016316. http://dx.doi.org/10.1103/PhysRevE.85.016316, URL https://link.aps.org/doi/10.1103/PhysRevE.85.016316.

Sidle, R.C., Nilsson, B., Hansen, M., Fredericia, J., 1998. Spatially varying hydraulic and solute transport characteristics of a fractured till determined by field tracer tests, funen, Denmark. Water Resour. Res. 34 (10), 2515–2527. http://dx.doi.org/10.1029/98WR01735, arXiv:https://agupubs.onlinelibrary.wiley.com/doi/pdf/10.1029/98WR01735.

Srzic, V., Cvetkovic, V., Andricevic, R., Gotovac, H., 2013. Impact of aquifer heterogeneity structure and local-scale dispersion on solute concentration uncertainty. Water Resour. Res. 49 (6), 3712–3728. http://dx.doi.org/10.1002/wrcr.20314, arXiv:https://agupubs.onlinelibrary.wiley.com/doi/pdf/10.1002/wrcr.20314.

Stauffer, D., Aharony, A., 1994. Percolation Theory: An Introduction, Vol. 46. http://dx.doi.org/10.1063/1.2808877.

Talon, L., Ollivier-Triquet, E., Dentz, M., Bauer, D., 2023. Transient dispersion regimes in heterogeneous porous media: On the impact of spatial heterogeneity in permeability and exchange kinetics in mobile–immobile transport. Adv. Water Resour. 174, 104425. http://dx.doi.org/10.1016/j.advwatres.2023.104425, URL https://www.sciencedirect.com/science/article/pii/S030917082300060X.

Tyukhova, A.R., Kinzelbach, W., Willmann, M., 2015. Delineation of connectivity structures in 2-D heterogeneous hydraulic conductivity fields. Water Resour. Res. 51 (7), 5846–5854. http://dx.doi.org/10.1002/2014WR015283, arXiv:https://agupubs.onlinelibrary.wiley.com/doi/pdf/10.1002/2014WR015283.

Tyukhova, A.R., Willmann, M., 2016. Connectivity metrics based on the path of smallest resistance. Adv. Water Resour. 88, 14–20. http://dx.doi.org/10.1016/j.advwatres.2015.11.014.

Western, A.W., Blöschl, G., Grayson, R.B., 2001. Toward capturing hydrologically significant connectivity in spatial patterns. Water Resour. Res. 37 (1), 83–97. http://dx.doi.org/10.1029/2000WR900241.

Willmann, M., Carrera, J., Sánchez-Vila, X., 2008. Transport upscaling in heterogeneous aquifers: What physical parameters control memory functions? Water Resour. Res. 44 (12), http://dx.doi.org/10.1029/2007WR006531, arXiv:https://agupubs.onlinelibrary.wiley.com/doi/pdf/10.1029/2007WR006531.

Zappa, G., Bersezio, R., Felletti, F., Giudici, M., 2006. Modeling heterogeneity of gravel-sand, braided stream, alluvial aquifers at the facies scale. J. Hydrol. 325 (1), 134–153. http://dx.doi.org/10.1016/j.jhydrol.2005.10.016, URL https://www.sciencedirect.com/science/article/pii/S0022169405005391.

Zarlenga, A., Fiori, A., 2015. Advective transport through three-dimensional anisotropic formations of bimodal hydraulic conductivity. Transp. Porous Media 107, 573–593. http://dx.doi.org/10.1007/s11242-015-0455-3.

Zarlenga, A., Jankovi ć, I., Fiori, A., Dagan, G., 2018. Effective hydraulic conductivity of three-dimensional heterogeneous formations of lognormal permeability distribution: The impact of connectivity. Water Resour. Res. 54 (3), 2480–2486. http://dx.doi.org/10.1002/2017WR022141.

Zinn, B., Harvey, C.F., 2003. When good statistical models of aquifer heterogeneity go bad: A comparison of flow, dispersion, and mass transfer in connected and multivariate Gaussian hydraulic conductivity fields. Water Resour. Res. 39 (3), http://dx.doi.org/10.1029/2001WR001146.